Asymmetric flow of polymer solutions around microfluidic cylinders: Interaction between shear-thinning and viscoelasticity

Journal of Non-Newtonian Fluid Mechanics 278 (2020) 104250

Contents lists available at ScienceDirect

Journal of Non-Newtonian Fluid Mechanics

journal homepage: www.elsevier.com/locate/jnnfm

Asymmetric flow of polymer solutions around microfluidic cylinders: Interaction between shear-thinning and viscoelasticity

Simon J. Haward*, Cameron C. Hopkins, Amy Q. Shen

Okinawa Institute of Science and Technology Graduate University, 1919-1 Tancha, Onna-son, Okinawa 904-0495, Japan

ARTICLE INFO

MSC:
00-01
99-00

Keywords:
Polymer solution
Viscoelasticity
Shear-thinning
Microfluidics
Cylinder
Flow modification

ABSTRACT

Viscoelastic flow around a cylinder is a model problem representing a wide range of relevant industrial processing and biological applications. Reducing the cylinder to microscopic dimensions conveniently enables the problem to be examined in the absence of inertia. Recently, we have developed glass microfluidic geometries containing long and slender, yet rigidly fixed, microfluidic cylinders, which present a low blockage ratio $\beta = 2r/W = 0.1$, where $r = 20$ μm is the cylinder radius and $W = 400$ μm is the channel width. Using a shear-banding viscoelastic wormlike micellar (WLM) solution, we showed how the flow around such a cylinder could destabilize beyond a critical Weissenberg number ($Wi = \lambda U/r$, where λ is a characteristic time of the fluid and U is the average flow velocity), resulting in the asymmetric division of the fluid around either side of the cylinder [Haward *et al, Soft Matter* **15**:1927]. In the present work we investigate this flow instability in greater detail using a range of polymer solutions formulated from hydrolyzed poly(acrylamide) (HPAA) dissolved at different concentrations in deionized water. The test fluids present a range of shear-thinning responses under steady shear, and also a wide variety of characteristic times. At low HPAA concentrations, the flow around the cylinder remains essentially symmetric for all *Wi*, but as the concentration increases, so does the maximum degree of the flow asymmetry observed with increasing *Wi*. Interestingly, at intermediate concentrations, the flow can resymmetrize at very high *Wi*. We understand these effects by considering simultaneously both the degree of shear-thinning of the fluid and the imposed *Wi*, and our analysis shows that both strong shear-thinning and high elasticity are required for the formation of strongly asymmetric flows. Our results represent the first report of this highly asymmetric flow state in polymer solutions, showing that it is a general phenomenon and not only specific to WLM. Our analysis provides a clear insight into the origins of this unusual flow state and may also be relevant to understanding other instances of asymmetries arising in shear-thinning viscoelastic flows.

1. Introduction

A circular cylinder is arguably the most fundamental model for a generic obstacle in a flow, also representing aspects of flows around particles, droplets and bubbles, and can therefore provide insight into a wide range of non-Newtonian flow phenomena [1,2]. Accordingly, the viscoelastic flow around cylinders is a well-studied problem both experimentally [3–10] and computationally [9,11–13], and is considered as one of the benchmark viscoelastic flows. Reducing the size of the cylinder to the microfluidic scale allows the problem to be examined in the absence of confounding inertial effects (i.e. Reynolds numbers $Re \ll 1$) while also permitting access to regimes of much higher elasticity (Weissenberg numbers $Wi \gg 1$) than possible in traditional macroscale systems [14–25]. Studying the viscoelastic flow around microscopic cylinders has relevance to a few specific problems including understanding biolocomotion of ciliated or flagellated organisms in mucosal fluids [26], and coating of fibres and fibrous materials with resins or polymeric cladding.

Recently, we developed microfluidic cylinder geometries fabricated from fused silica glass by the technique of selective laser induced etching (SLE) [27–29]. In contrast to microfluidic geometries typically fabricated by soft lithography, SLE permits the fabrication of microchannels containing extremely long and slender cylinders, that remain essentially rigid due to the high modulus of the glass material, see Fig. 1. The device shown consists of a rectangular channel with height $H = 2$ mm, width $W = 0.4$ mm containing a cylinder of radius $r = 20$ μm that spans the full height of the channel. Compared with most microfluidic geometries, the channel has a much higher aspect ratio $\alpha = H/W = 5$, which we have shown provides a good approximation to two-dimensional (2D) flow along the length of the cylinder [28]. The blockage of the channel

* Corresponding author.
E-mail address: simon.haward@oist.jp (S.J. Haward).

https://doi.org/10.1016/j.jnnfm.2020.104250
Received 14 October 2019; Received in revised form 10 January 2020; Accepted 13 February 2020
Available online 19 February 2020

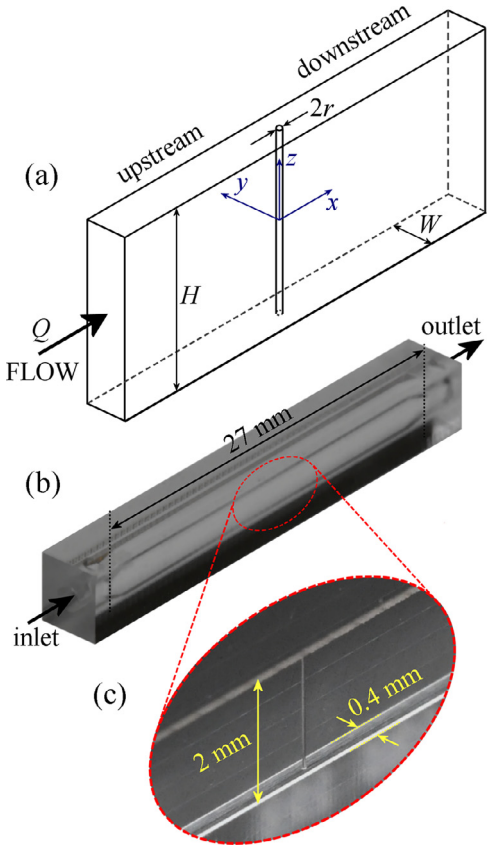

Fig. 1. Illustrations of the microfluidic device containing a single slender circular cylinder. (a) A schematic drawing of the device indicating the important characteristic dimensions (channel width W, height H and cylinder diameter $2r$), the flow direction at imposed volumetric flow rate Q, and the coordinate system with origin at the geometric centre of the cylinder. (b) A photograph of a microchannel, and (c) a magnified view of the region around the microcylinder obtained by removing one side-wall of the channel. The channel dimensions are $W = 0.4$ mm and $H = 2$ mm and $r = 20$ μm. The total length of the channel between the inlet and the outlet is $L = 27$ mm and the cylinder is located 13.5 mm downstream of the inlet.

by the presence of the cylinder is also relatively minor (blockage ratio $\beta = 2r/W = 0.1$) compared with most experimental microfluidic flow geometries (typically $\beta \gtrsim 0.5$, e.g. [16,19,21]). In contrast to most high β microscale (and some macroscale) experiments in which high Wi result in instabilities occurring upstream of the cylinder [9,16,18,19,21], we have shown that the lower degree of confinement has a significant impact on the non-Newtonian fluid dynamics. A low value of β reduces the importance of the squeezing flow between the cylinder and the side walls, which allows the strongly-deforming extensional flow at the leading and trailing stagnation points of the cylinder to play a more dominant role and leads to more interesting dynamics downstream of the cylinder [28,29].

So far, our investigations utilizing these novel microfluidic geometries have involved the steady flow of essentially constant viscosity viscoelastic polystyrene solutions [28], and also the flow of intensely shear-thinning (in fact shear-banding, [30,31]) viscoelastic wormlike micellar (WLM) solutions [29]. One of the most intriguing observations we have made involves the formation of a steady flow asymmetry in the WLM solution. Above a critical value of the Weissenberg number $Wi_c \approx 60$, the flow bifurcated to an asymmetric state in which the fluid passed preferentially around one side of the cylinder (as illustrated in Fig. 2). By contrast, in a constant viscosity polymer solution, although we observed extremely long elastic wakes extending up to ≈ 300 cylinder radii downstream of the cylinder, the flow field remained

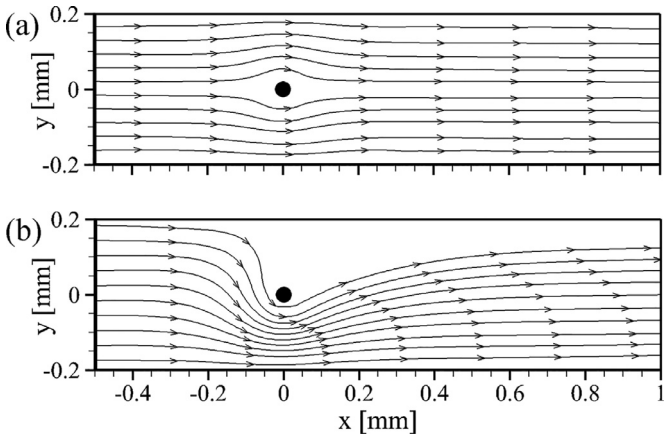

Fig. 2. Streamline plots determined from micro-particle image velocimetry measurements made for flow around a slender microfluidic cylinder, illustrating (a) symmetric flow of a Newtonian fluid at low Reynolds number, $Re < 10^{-3}$, and (b) a strongly asymmetric flow of a shear-banding viscoelastic wormlike micelle solution at low Reynolds number, $Re < 10^{-6}$, but high Weissenberg number $Wi \approx 180$.

essentially laterally symmetric for all Wi, with only relatively weak bending of streamlines near the upstream stagnation point at the highest Wi tested [28]. We speculated that generation of this flow asymmetry in the WLM solution required a combination of micelle deformation (hence enhanced elongational stress) in the wake downstream of the cylinder, and shear-thinning between the cylinder and the channel side walls, although other possiblilities are that entanglement effects and/or shear-banding may also be important. We note that Dey *et al* reported similar asymmetric flow patterns for flows of WLMs around a millimetre scale cylinder also at a low blockage ratio, $\beta = 0.024$ [32]. They used a strongly shear-thinning fluid with a high zero-shear-rate viscosity $\eta_0 \approx 200$ Pa s and a long relaxation time $\lambda \approx 30$ s, which allowed high Weissenberg numbers to be reached with negligible inertia, even though the lengthscale was relatively large. However, in that case the cylinder had significant flexibility and under flow deflected laterally from its equilibrium position, offering a ready explanation for the asymmetry. By contrast, in our experimental setup the cylinder remains firmly located on the central axis of the channel. In fact, in the experiments of Dey et al, it is likely that it was the onset of fluid flow asymmetry that drove the cylinder off-axis *via* the viscoelastic fluid-structure interaction [32–34].

In this work, we employ the same glass microfluidic cylinder geometry as used in our previous studies (see Fig. 1) to perform a systematic study of the steady flow asymmetry illustrated by Fig. 2b. We formulate and rheologically characterize a range of semi-dilute entangled polymer solutions composed of the industrially important polyelectrolyte hydrolyzed poly(acrylamide). The range of fluid rheological properties allows us to decouple and understand the effects of shear-thinning and fluid elasticity. Our results constitute the first report of such asymmetric flow patterns of polymer solutions around cylinders, confirming that this phenomenon is not particular to some aspect of WLM rheology (such as shear-banding or fast-breaking relaxation mechanisms), but is a more general phenomenon likely common to a range of shear-thinning viscoelastic fluids. The analysis of our results lends strong support to our earlier speculative hypothesis regarding the instability mechanism based on an interaction between elasticity in the wake and shear-thinning around the sides of the cylinder. The mechanism we propose may be relevant to understanding flow asymmetries in other fundamental flow geometries (like T-junctions, X-junctions and contractions) when both shear-thinning and elasticity are important, and may be insightful for understanding why viscoelastic fluids select preferred paths through complex tortuous geometries such as porous media for example (e.g. [35,36]).

Table 1
Parameters extracted from the shear and extensional rheometry performed on the shear-thinning solutions of HPAA in deionized water at 25°C.

c [ppm]	η_0 [Pa s]	η_∞ [mPa s]	$\dot{\gamma}^*$ [s^{-1}]	n	a	λ [ms]
50	0.09	1.4	0.073	0.40	1.83	8
100	0.21	1.8	0.068	0.38	1.53	32
200	0.68	2.0	0.025	0.38	1.54	78
300	1.33	2.2	0.017	0.37	1.45	140
500	3.67	3.0	0.011	0.33	1.39	245
1000	12.5	5.0	0.011	0.25	1.05	380
3000	61.6	9.0	0.010	0.21	0.78	930

2. Materials and methods

2.1. Microfluidic device

The microfluidic cylinder device employed in the experiments is the same as that used in our prior studies and described in detail therein [28,29]. The device was fabricated by SLE in fused silica glass using a commercial "LightFab" three-dimensional (3D) printer (LightFab GmbH, Germany) [27,37,38]. The schematic diagram in Fig. 1a indicates the Cartesian coordinate system employed, with origin at the centre of the cylinder, the flow direction and the labelling of the principal dimensions. Photographs of similar devices to the one used in the experiments are shown in Fig. 1b,c. Note that, for purely illustrative purposes, the device shown in Fig. 1c has had one of the channel side walls removed to allow the acquisition of a high quality oblique angle photograph of the cylinder inside the channel.

2.2. Test fluids

The viscoelastic test solutions are composed of a high molecular weight ($M_w = 18$ MDa), commercial sample of partially hydrolyzed poly(acrylamide) (HPAA, Polysciences Inc.), with a degree of hydrolysis between 30 and 40%. The polymer is dissolved in deionized (DI) water over a range of concentrations $50 \leq c \leq 3000$ ppm (by weight). Since HPAA is a polyelectrolyte, the molecule is expected to be highly expanded in DI water due to the dissociation of the charges on the hydrolzed groups. The viscosities of the fluids have been measured at 25°C in steady shear using an Anton-Paar MCR 502 stress-controlled rheometer fitted with a stainless steel double-gap geometry. The results are presented in terms of both stress σ *versus* shear rate $\dot{\gamma}$ (Fig. 3a) and viscosity η *versus* $\dot{\gamma}$ (Fig. 3b). The fluids are all shear-thinning with flow curves that are well-described by the Carreau–Yasuda generalized Newtonian fluid (GNF) model (shown in the plots by the correspondingly-coloured solid lines):

$$\eta = \eta_\infty + \frac{\eta_0 - \eta_\infty}{[1 + (\dot{\gamma}/\dot{\gamma}^*)^a]^{(1-n)/a}}, \tag{1}$$

where η_∞ is the infinite-shear-rate viscosity, η_0 is the zero-shear-rate viscosity, $\dot{\gamma}^*$ is the characteristic shear rate for the onset of shear-thinning, n is the "power-law exponent" in the shear-thinning region and a is a dimensionless fitting parameter that controls the rate of the transition between the constant viscosity and the shear-thinning regions. Values for all of these parameters are provided in Table 1. The log-log plot inserted in Fig. 3b shows η_0/η_s as a function of the HPAA concentration, where $\eta_s = 0.89$ mPa s is the viscosity of the solvent (DI water) at 25°C. The slope is close to 3/2, which is indicative of the semi-dilute entangled regime for polyelectrolytes in the absence of added counterions [39].

For the purposes of later experimental data analysis we also define here a "shear-thinning parameter" S, which quantifies the importance of shear-thinning in entangled systems [40,41]:

$$S \equiv 1 - \frac{\eta_c}{\eta(\dot{\gamma})}, \tag{2}$$

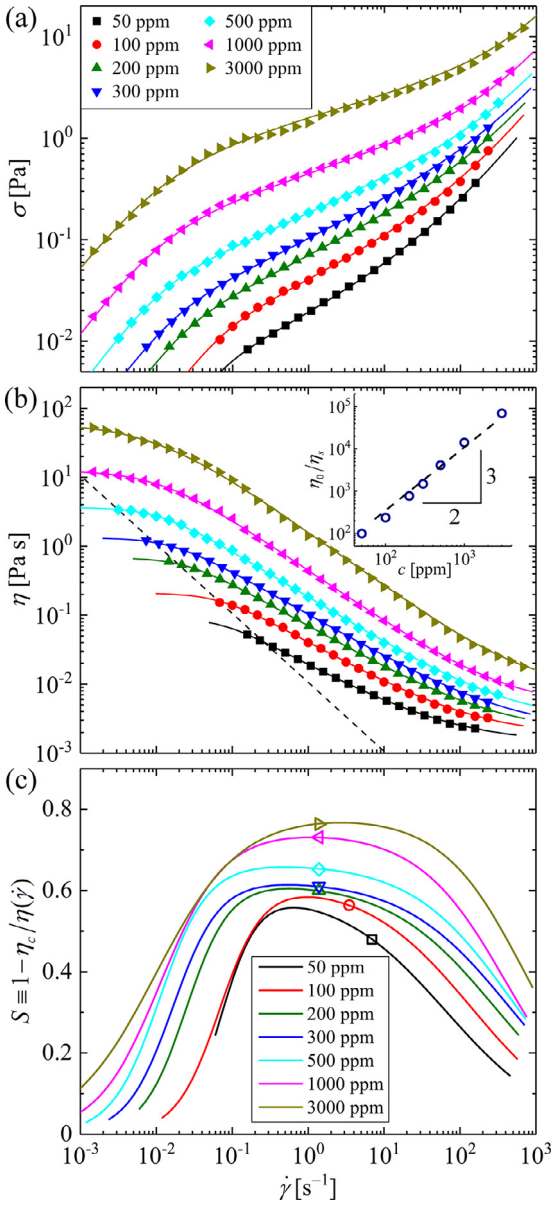

Fig. 3. Rheological characterization of the HPAA-based polymeric test solutions carried out in steady shear at 25°C using an Anton-Paar MCR 502 stress-controlled rheometer fitted with a stainless steel double-gap geometry. (a) Stress σ and (b) viscosity η as function of the imposed shear rate $\dot{\gamma}$. The experimental data points are fitted with a Carreau-Yasuda GNF model (see main text), shown by the correspondingly-coloured solid lines. The insert in (b) shows the zero shear viscosity η_0 obtained from the Carreau-Yasuda model fit divided by the solvent viscosity η_s, plotted as a function of the polymer concentration. The slope of 1.5 indicates that the fluids are in the semi-dilute entangled regime. The diagonal dashed line in (b) indicates the minimum sensitivity of the measurement, based on 10 × the minimum torque sensitivity of the rheometer (0.1 μN m). (c) The "shear-thinning parameter" S (see main text for description) as a function of the imposed shear rate, computed from the Carreau-Yasuda fits to the steady shear rheology. The open symbols mark the value of S at the minimum characteristic shear rate accessed in the cylinder channel flow experiments.

where $\eta_c \equiv d\sigma/d\dot{\gamma}$ is the tangent viscosity (or "consistency") [42], and $\eta(\dot{\gamma}) \equiv \sigma/\dot{\gamma}$ is the shear rate-dependent viscosity shown in Fig. 3b. Putting the expressions for η_c and $\eta(\dot{\gamma})$ into Eq. (2), S can be expressed alternatively as [41]:

$$S = 1 - \frac{d \ln \sigma}{d \ln \dot{\gamma}}, \tag{3}$$

which is simply 1 minus the slope of the stress *versus* shear rate plot in Fig. 3a, and is easily evaluated from the experimental flow curve data. If a fluid behaves in a pseudo-Newtonian way, such that there is no shear-thinning, then $d\ln\sigma/d\ln\dot{\gamma} = 1$ and $S = 0$. For a general shear-thinning fluid, $0 < d\ln\sigma/d\ln\dot{\gamma} < 1$ and S attains a positive value $0 < S < 1$. For a shear-banding fluid such as a WLM solution exhibiting a stress plateau where $\eta \sim 1/\dot{\gamma}$ and $\eta_c = 0$, S can attain its maximum value of unity.

In Fig. 3c, we show S *versus* $\dot{\gamma}$, evaluated using the Carreau–Yasuda fits to the experimental flow curves. We observe that S is close to zero at low shear rates (i.e. the fluid is only weakly shear-thinning) and increases to a maximum at some intermediate shear rate as the consistency decreases. At higher shear rates, S decreases again as the high shear rate plateau in viscosity is approached. In general, the curves are all of similar shape, but S becomes increasingly large over a wider range of shear rates as the HPAA concentration increases.

The relaxation times (λ) of the fluids at 25°C were determined in a uniaxial extensional flow by measuring the diameter as a function of time ($D(t)$) of the liquid bridge generated in a capillary thinning extensional rheology device (Haake CaBER 1, Thermo Scientific) [43,44], see Fig. 4a. The CaBER device was fitted with plates of diameter $D_0 = 6$ mm, the initial gap between the plates was 1 mm, and the plates were separated to a final gap of 6 mm by linear displacement at a rate of 0.1 m s^{-1}. All of the test fluids display clear "elastocapillary" behaviour where D/D_0 decays exponentially in time, and from which the relaxation time can be determined from a fit of the form: $D(t)/D_0 \sim \exp[-t/3\lambda]$. The values of λ thus determined are provided in Table 1. Within the elastocapillary thinning regime, the CaBER measurement can also be used to estimate the extensional viscosity of the fluid: $\eta_E \approx -\gamma/(dD(t)/dt)$, where $\gamma = 72.0$ mN m^{-1} is the surface tension of the DI water solvent at 25°C. We used a pendant drop tensiometer (Attension Theta, Biolin Scientific) to confirm that there was negligible difference between the surface tension of the HPAA solutions and the solvent. The extensional viscosity is plotted as a function of the accumulated Hencky strain: $\varepsilon_H = 2\ln(D_0/D(t))$ in Fig. 4b. Clearly, all of the test fluids show strain-hardening, with an extensional viscosity that increases mildly with the Hencky strain. It is perhaps more instructive to consider the Trouton ratio of the fluid, which (since the flow in the CaBER device is essentially shear free) we define $Tr = \eta_E/\eta_0$, see Fig. 4b. Interestingly, the most concentrated HPAA solution (3000 ppm) displays the lowest Trouton ratio, which appears to plateau to a value of $Tr \approx 10$ at high ε_H. The Trouton ratio progressively increases as the HPAA concentration is decreased, saturating at the highest dilutions, for which values of $Tr \approx 100$ are approached at the highest Hencky strains. Accordingly, it is clear that these fluids show a significant non-Newtonian elastic response in uniaxial extensional flow; the Trouton ratio expected for a Newtonian fluid subjected to uniaxial extensional deformation is $Tr = 3$.

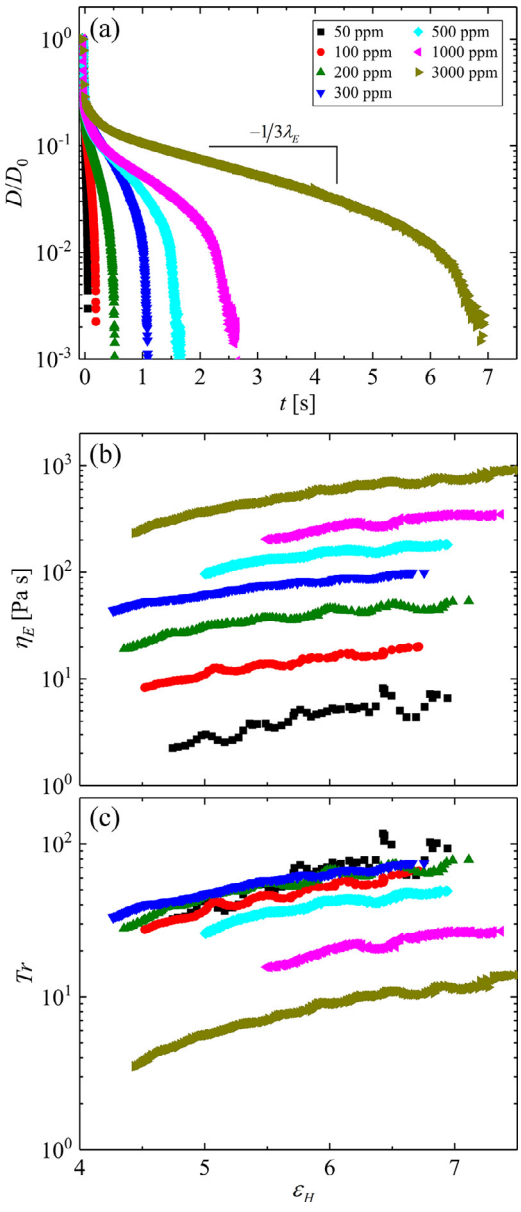

Fig. 4. Characterization of the extensional response of the polymeric test fluids at 25°C using a capillary-breakup extensional rheometer (CaBER 1, Thermo Haake). (a) Normalized filament diameter D/D_0 as a funtion of time, from which the extensional relaxation time λ can be determined within the exponentially-decaying elasto-capillary thinning regime. (b) Extensional viscosity η_E, and (c) Trouton ratio $Tr = \eta_E/\eta_0$ as a function of the accumulated Hencky strain ε_H.

2.3. Flow control and dimensionless numbers

The test fluids are driven through the microfluidic cylinder device at precisely controlled volumetric flow rates Q using two neMESYS low pressure syringe pumps (Cetoni, GmbH) with 29:1 gear ratios. One of the pumps is used to infuse fluid into the device while the second pump withdraws fluid at an equal and opposite rate from the downstream outlet. The pumps are fitted with Hamilton Gastight syringes of appropriate volumes such that the specified "pulsation free" dosing rate is always exceeded even at the lowest imposed Q. Connections between the syringes and the microfluidic devices are made using flexible silicone tubing.

The Reynolds number is used to describe the relative strength of inertial to viscous forces in the flow, and is defined using the lengthscale (radius r) associated with the microfluidic cylinder:

$$Re = \frac{\rho U r}{\eta_0}, \tag{4}$$

where $U = Q/WH$ is the average flow velocity in the microchannel and $\rho = 997$ kg m^{-3} is the fluid density (assumed to be equal to the DI water solvent). We use the zero-shear-rate viscosity η_0 as a representative value in the denominator of Eq. (4) since the cylinder is located on the channel centerline where the shear rate is zero. In the experiments to be described in the following, the Reynolds number does not exceed a value of $Re \approx 0.05$, even for the most dilute and low viscosity fluid at the highest imposed flow rate. Hence, inertial effects in the flows to be discussed can be ignored.

We use a characteristic Weissenberg number to describe the relative strength of elastic to viscous forces in the polymeric flow around the cylinders:

$$Wi = \frac{\lambda U}{r}, \tag{5}$$

where U/r is a characteristic deformation rate for the flow, defined by the nominal velocity gradient in the cylinder wake. For $Wi \lesssim 1$, we expect polymer molecules to relax faster than they are being deformed and

an essentially Newtonian-like response of the fluid. For $Wi \gtrsim 1$, polymer molecules will be deformed in the velocity gradient leading to the generation of additional elastic stresses in the wake that can modify the flow field (see e.g. Ref. [28]).

The elasticity number describes the relative strength of elastic to inertial forces in the polymeric flow:

$$El = \frac{Wi}{Re} = \frac{\lambda\eta}{\rho r^2}. \quad (6)$$

For the polymer solutions employed here, the elasticity number varies in the range $10^3 \lesssim El \lesssim 10^8$, clearly indicating that (for $Wi \gtrsim 1$) these will be elasticity-dominated flows.

The importance of shear-thinning in the microfluidic cylinder geometry is quantified using Eq. (3) evaluated at a nominal value of the wall shear rate in the gap between the cylinder and the channel side wall, $\dot{\gamma}_{w,gap}$. The width of each gap is $W_{gap} = 0.5W(1-\beta)$, and based on equal division of the fluid between the gaps, the average flow velocity in each gap will be $U_{gap} = U/(1-\beta)$. Assuming fully-developed 2D Poiseuille flow, the nominal wall shear rate in the gap is thus $\dot{\gamma}_{w,gap} = 6U_{gap}/W_{gap} = 6U/0.5W(1-\beta)^2$, which can be reduced to $\dot{\gamma}_{w,gap} \approx 6U/0.5W$ since β is small. Note that for information, and to aid later discussion, the minimum value of $\dot{\gamma}_{w,gap}$ accessed for each fluid in the cylinder channel experiments is marked by the open symbols included on the plot of *S versus* $\dot{\gamma}$ shown in Fig. 3c.

2.3.1. Microparticle image velocimetry

The flow of the HPAA solutions around the microfluidic circular cylinder is quantified using a volume illumination μ-PIV system (TSI Inc., MN). For these experiments, the test fluids are seeded with a low concentration ($c_p \approx 0.02$ wt%) of 2 μm diameter fluorescent tracer particles (PS-FluoRed-Particles, Microparticles GmbH) with excitation/emission wavelength 530/ 607 nm. The $z = 0$ plane of the flow geometry is brought into focus on an inverted microscope (Nikon Eclipse Ti) with a 5 ×, NA= 0.15 numerical aperture Nikon PlanFluor objective lens. The corresponding measurement depth over which microparticles contribute to the determination of the velocity field is $\delta_m \approx 125\,\mu$m (or $\approx H/16$) [45]. Particle fluorescence is induced by excitation with a dual-pulsed Nd:YLF laser (wavelength of 527 nm, time separation between pulses Δt) and a high speed imaging sensor (Phantom MIRO) operating in frame-straddling mode captures pairs of particle images in synchrony with the laser pulses. At each flow rate examined, the time Δt is set so that the average displacement of particles between the two images in each pair is ≈ 4 pixels. Since in the present experiments we only examine steady flows, 50 image pairs are processed using an ensemble average cross-correlation PIV algorithm (TSI Insight 4G). A recursive Nyquist criterion is employed with a final interrogation area of 16 × 16 pixels to enhance the spatial resolution and obtain 2D velocity vectors $\boldsymbol{v} = (u, v)$ spaced on a square grid of 12.8 × 12.8 μm. Further image analysis, generation of contour plots and streamline traces is performed using the software Tecplot Focus (Tecplot Inc., WA).

3. Results and discussion

In this section, we proceed to examine the flow of the polymeric test solutions around the single microscopic cylinder contained inside the flow channel. Representative flow fields measured for a few of the HPAA solutions are shown for a range of *Wi* and *S* values in Fig. 5. The quoted values of *S* are obtained by evaluating Eq. (3) at the nominal wall shear rate in the gaps between the cylinder and the side walls, as described in Section 2.3. At the lowest concentrations of HPAA, i.e. 50 ppm and 100 ppm (Fig. 5a), the flow remains essentially laterally symmetric about $y = 0$, with fluid passing above and below the cylinder almost equally at all *Wi*. However, as *Wi* increases, we observe the development of an increasingly long downstream wake where the fluid maintains a low velocity on the channel centerline even many cylinder radii downstream. This is associated with the elastic response of the fluid due to the stretching and orientation of polymer molecules in the velocity gradient downstream of the trailing stagnation point, resulting in high elastic stresses and a localized increase in the extensional viscosity (i.e. strain-hardening) [11,28].

At intermediate concentrations of HPAA (e.g. 200 ppm, Fig. 5b), the flow field appears laterally symmetric at the lowest $Wi = 0.41$, but exhibits a clear asymmetry at certain intermediate *Wi* values, where fluid may pass preferentially either above or below the cylinder. Interestingly, the lateral symmetry is completely regained as the Weissenberg number becomes higher, even though the fluid exhibits a strong elastic response to the streamwise velocity gradient in the wake. A qualitatively similar sequence of behaviour is also observed at higher intermediate HPAA concentrations (e.g. 500 ppm, Fig. 5c), although in this case the asymmetry around the cylinder continues to intensify as *Wi* is increased to higher values, and we only observe a partial resymmetrization at the highest imposed *Wi* values.

At the highest HPAA concentrations tested, e.g. 1000 ppm (Fig. 5d), again the flow appears quite symmetric at the lowest imposed $Wi = 0.79$. With increasing *Wi*, a weak elastic downstream wake develops ($Wi = 3.96$) before the flow becomes strongly and dramatically asymmetric at higher *Wi*. In this case the asymmetry remains intense up to the highest Weissenberg numbers tested.

The asymmetric flow patterns presented in Fig. 5d at the higher values of *Wi* are of strikingly similar form to those presented in earlier works with wormlike micellar solutions around rigid [29] and deformable [32] circular cylinders. However, this is the first report of such asymmetries arising in solutions of linear polymers. This observation therefore immediately discounts any special property of WLM fluids (e.g. a stress-plateau in the flow curve, or the ability of micelles to restructure under flow) as causing the instability.

The degree of lateral asymmetry in the flow around the cylinder is quantified using the same asymmetry parameter employed in our previous work with WLM solutions [29]:

$$I = \frac{|u_1 - u_2|}{(u_1 + u_2)}, \quad (7)$$

where u_1 and u_2 are the streamwise fluid velocities measured at the midpoints between the cylinder and the top and bottom side walls, respectively. By this measure of asymmetry, $I = 0$ implies perfectly symmetric flow, while $I = 1$ implies that *all* of the fluid passes on just one side of the cylinder.

The asymmetry parameter *I* is shown as a function of *Wi* in Fig. 6. As described qualitatively above, Fig. 6 shows that for the lowest HPAA concentrations the degree of asymmetry remains low $I \lesssim 0.1$ for all *Wi*. As the HPAA concentration is increased in an intermediate range $200 \leq c \leq 500$ ppm, the asymmetry passes through a peak as the Weissenberg number is initially increased, but then tends back down towards a value of zero for very high *Wi*. At the highest HPAA concentrations tested, the flow becomes asymmetric as the *Wi* is increased and remains highly asymmetric even at the highest *Wi* achieved. By plotting the same data with *Wi* on a logarithmic scale (Fig. 6b) some interesting additional features are apparent. It is clear that the maximum value of the asymmetry parameter I_{max} increases with the polymer concentration. Also (as a general trend) the critical Weissenberg number Wi_c for the onset of asymmetry increases with the polymer concentration, as does the Weissenberg number above which the flow begins to resymmetrize. Some of these observations seem quite intuitive, for instance the existence of a critical value of *Wi* for the onset of asymmetry (which is $Wi_c \sim 1$ for the lower concentration fluids that exhibit an increase in *I*), suggests that the asymmetry is related to elasticity. Also, the increasing value of I_{max} with increasing polymer concentration seems logical. However, certain observations are perhaps more surprising, for instance why does the value of Wi_c increase with polymer concentration? Also, if the asymmetry is an elastic effect, why in some cases does the flow recover symmetry as the Weissenberg number, hence elasticity, is increased? Typically, for flows at high *Wi* and low *Re,* an increasing *Wi*

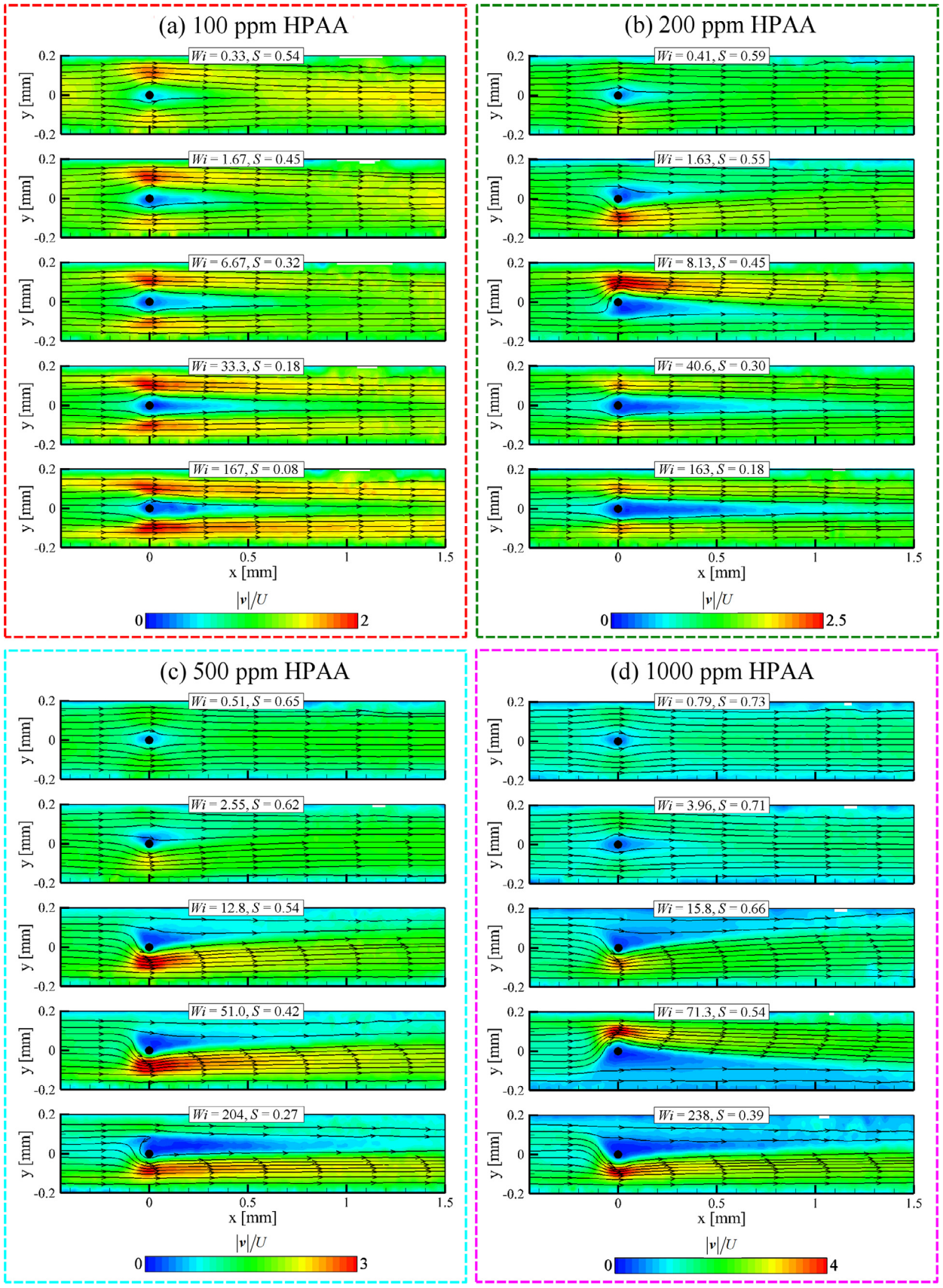

Fig. 5. Flow fields measured around the cylinder with HPAA solutions at various concentrations and over a range of imposed *Wi* indicated in the images. (a) 100 ppm HPAA, (b) 300 ppm HPAA, (c) 500 ppm HPAA, (d) 1000 ppm HPAA. The colour contours indicate the normalized velocity magnitude, $|\boldsymbol{v}|/U$, while superimposed streamlines indicate the direction of fluid motion. In all cases, the Reynolds number is $Re < 0.01$.

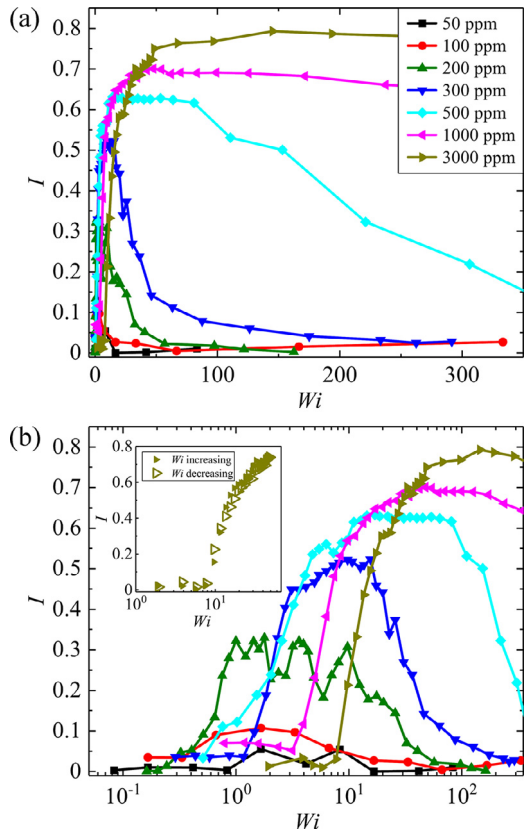

Fig. 6. Asymmetry parameter I (see text) as a function of the imposed Weissenberg number, shown on (a) linear-linear, and (b) linear-log axes. The insert plot in (b) shows a test for hysteresis using the most concentrated (3000 ppm) HPAA solution, confirming that the symmetric-asymmetric transition is not hysteretic.

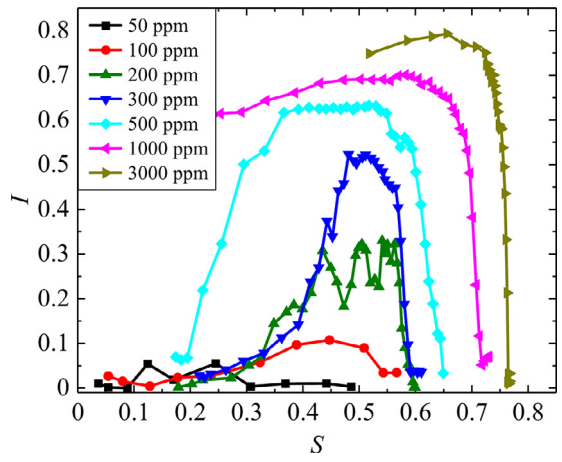

Fig. 7. Asymmetry I as a function of the shear-thinning parameter S.

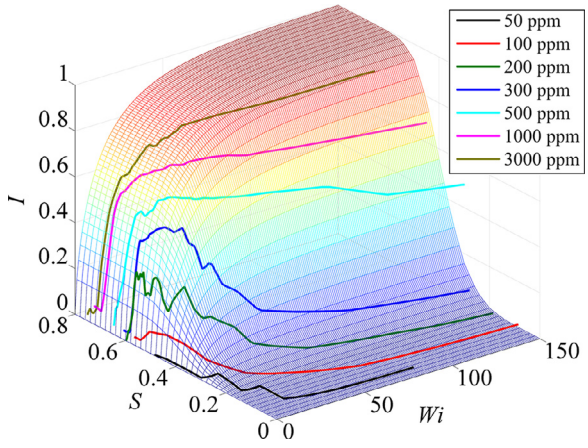

Fig. 8. Asymmetry parameter I as a function of S and the imposed Weissenberg number, *Wi*. The colored lines represent the trajectories of the various test fluids through the three-dimensional space. The continuous surface is formed by fitting the trajectories of the fluids with the product of two sigmoidal functions (see text for details). (For interpretation of the references to color in this figure legend, the reader is referred to the web version of this article.)

leads to increasing nonlinearity, often resulting in time-dependent or even chaotic-like (elastically turbulent) states (e.g. [17,46,47]).

As a side note, the inserted plot on Fig. 6b shows the result of a test for hysteresis in the transition to asymmetry carried out using the most concentrated 3000 ppm HPAA solution. For this experiment, the Weissenberg number was quasistatically varied following a stepwise triangular profile from an initial value of $Wi_i = 1.94$ (below the transition) up to a maximum value of $Wi_m = 48.4$ (above the transition) and back to a final value $Wi_f = Wi_i = 1.94$. The stepwise increments were each of $Wi = 1.94$ and each step was maintained for 45 s in order that a steady state was achieved. We consider that if the transition was related to polymer entanglements then we should see hysteresis in the resulting plot of I *versus* *Wi* since once an asymmetry has arisen, there would be an additional force present due to entanglements pulling the fluid to one side of the cylinder. Since there is clearly no hysteresis evident in the transition for the 3000 ppm HPAA solution (the most entangled that we studied), we believe this discounts forces that arise due to intermolecular entanglements as playing a significant role in driving this instability.

Following our intuition that shear-thinning plays a prominent role in causing the asymmetric flows we observe around the cylinder, in Fig. 7 we consider how the asymmetry I depends on the shear-thinning parameter S. As discussed above, in the microfluidic cylinder geometry we evaluate S at the average wall shear rate in the gaps between the cylinder and the channel side walls, see Section 2.3. The minimum values of these shear rates closely coincide to the peak value of S for each fluid, as shown by the open symbols plotted in Fig. 3c. Hence, in Fig. 7, as the flow rate (or *Wi*) is increased, S progresses from right to left of the plot (i.e. from high to low values). In our view, there is limited information to be gained from Fig. 7 when viewed in isolation. Perhaps two worthwhile observations to mention at this stage are (1) that flow asymmetries develop at high values of $S \gtrsim 0.5$, (2) resymmetrization of the flow field appears to occur as S becomes lower, although there is clearly some fluid dependence as to the value of S when resymmetrization commences and is complete.

We believe that only by considering both shear-thinning and elasticity simultaneously, can the transitions between symmetric and asymmetric flow fields be understood properly. In Fig. 8, we plot the trajectories of the test fluids through a three-dimensional $Wi - S - I$ state space. The trajectories of the test fluids (shown by the coloured lines) are seen to form a surface that can be fitted reasonably well with a simple function composed of two sigmoidal growth curves: $I = (1 - \exp[-(aWi)^b])(1 - \exp[-(cS)^d])$, where the fitting parameters $a = 0.035$ and $b = 0.56$ determine the onset and rate of growth of I along the *Wi*-direction, and $c = 2.4$ and $d = 5.4$ determine the onset and rate of growth of I along the S-direction. This surface naturally tends to a value of $I = 0$ as $Wi \to 0$ or $S \to 0$ and to a value of $I = 1$ when both *Wi* and S become large.

By studying the plots in Fig. 8 carefully, it becomes obvious why, for example the flow remains symmetric at lower HPAA concentrations. By following the trajectories of the black and red lines (50 ppm and 100 ppm HPAA, respectively), it is clear that at lower flow rates,

although shear-thinning is strong, the Weissenberg number is negligible. But, as the flow rate increases and Wi becomes appreciable, the shear-thinning decreases sharply and becomes negligible. On the contrary, for the highest concentrations of HPAA (e.g. 1000 ppm and 3000 ppm – magenta and gold lines, respectively), S remains high as the Weissenberg number also becomes large, and under these conditions strong flow asymmetries develop. At intermediate HPAA concentrations (e.g. 300 ppm, blue line), a regime can exist where the combination of shear-thinning and elasticity is sufficient to drive a flow asymmetry. But, as the flow rate is increased, the shear-thinning becomes weak, and the flow can recover symmetry even though elastic effects become increasingly strong. Clearly the generation of highly asymmetric flows requires both strong shear-thinning and high elasticity.

These results and analyses lend support to our earlier ideas regarding the mechanism for this instability [29]. First, an elastic wake downstream of the cylinder must be generated, so that a Weissenberg number $Wi \gtrsim 1$ is a requirement. We assume that the flow asymmetry is initiated by a small lateral fluctuation of the elastic wake, due to some form of random noise in the system. A fluctuation of the wake to one side of the cylinder will cause an increase in the flow resistance to that side, preventing fluid from passing that side of the obstacle (like partially closing a valve). By continuity, the flow rate must therefore increase on the opposite side of the cylinder. This imbalance in flow rate on either side of the cylinder means there is also an imbalance in the shear rate, and if the fluid is shear-thinning, an imbalance in the viscosity. Low flow rate ⇒ high viscosity while high flow rate ⇒ low viscosity, and the disparity in viscosity therefore serves to support the induced asymmetry, keeping the valve partially closed. Thus, it is possible for the asymmetry of the elastic downstream wake and the imbalance in shear rate around the sides of the cylinder to maintain each other in a self-sustaining feedback cycle.

The mechanism described above implies a few interesting scenarios. From a fluid rheological perspective, shear-thinning, but inelastic fluids with $Wi \equiv 0$ for all S would not be expected to display flow asymmetries. Interestingly, for any shear-thinning fluid with $0 < S < 1$, the shear stress around the cylinder should always decrease if the flow becomes asymmetric, which by itself suggests a rationalization for the asymmetry based on energy minimization considerations. However, we have conducted preliminary experiments with strongly shear-thinning but almost inelastic xanthan gum solutions and we were unable to drive the flow to become asymmetric, further supporting our proposal that the combination of shear-thinning *and* elasticity is required. Conversely, elastic, but constant viscosity fluids (like Boger fluids) with $S \equiv 0$ for all Wi would also not show flow asymmetries (our earlier work with dilute polystyrene solutions extending up to $Wi > 60$ already does support this [28]). From a geometrical standpoint, if the cylinder was truely unconfined (or the channel side walls were sufficiently far apart that the gap wall shear rate was always on the low shear rate plateau) an asymmetry would again not be expected (unfortunately, simple estimates show that this is a difficult scenario to test from a device fabrication point of view). At the other geometric extreme, if the cylinder confinement was made very high, it could be possible for the gap wall shear rate to be at the high shear rate plateau for all imposed Wi. However, at the necessary high blockage ratios, the extensional flow of fluid being squeezed through the gaps becomes important, leading to different instabilities upstream of the cylinder, as shown in several earlier microfluidic (and macroscale) studies (e.g. [9,16,19,21]). As a final point, we should mention that we see no reason for the instability we report here to be restricted to microscale geometries. Provided the relevant combination of geometric and fluid flow regimes are met then this asymmetry should be present for any lengthscale (as hinted at by the results of Dey et al. for flows of WLM's around milimeter-sized cylinders [32]). However, for an aqueous-based shear-thinning polymer solution with a short relaxation time, such conditions are most readily met at the microscale.

One experimental observation that is not clearly explained by the proposed instability mechanism is the progressive increase in the critical Weissenberg number Wi_c for the onset of asymmetry with increasing polymer concentration (see Fig. 6b). This may be explained by a shear-thinning in the relaxation time (see e.g., [48]). However, another possiblity that fits with our hypothesis could be the decrease in Trouton ratio with increasing polymer concentration (as shown in Fig. 4c) and consequently a relatively weaker strain-hardening in the wake of the cylinder as Wi is increased.

4. Conclusions

In this study we have examined the flow of a range of semidilute entangled polymer solutions with different shear-thinning characteristics and relaxation times past a microfluidic cylinder with low blockage ratio. Our intention was to shed light on the mechanism underlying an unusual asymmetric flow state previously observed in the flow of a particular shear-banding wormlike micellar solution through the same microfluidic device. The fact that we observe a very similar flow state forming in many of the polymer solutions we examined immediately confirms that such bifurcations are not due to some peculiarity of WLMs (like shear-banding or the ability to reform after breakage), and shows that this is a more general phenomenon, likely common to a range of complex fluids. Our data analysis, carried out in terms of quantifying the fluid elasticity in the wake of the cylinder and the degree of shear-thinning at the sides of the cylinder, strongly suggests that a combination of both elasticity and shear-thinning are necessary for the generation of the asymmetry. We suggest that an initial random lateral fluctuation of the elastic wake downstream of the cylinder causes an initial small imbalance in the flow rate (hence shear rate) either side of the cylinder. The resulting imbalance in viscosity due to the shear-thinning then leads to the asymmetry becoming self-sustaining.

We think that such a mechanism could help explain why complex fluids can select preferential paths through complex geometries (e.g. porous media models like cylinder arrays) and may also be helpful for understanding other instances of flow asymmetries arising in shear-thinning elastic liquids.

Declaration of Competing Interest

There are no conflicts of interest.

Acknowledgments

We gratefully acknowledge the support of the Okinawa Institute of Science and Technology Graduate University (OIST) with subsidy funding from the Cabinet Office, Government of Japan. S.J.H. and A.Q.S. also acknowledge funding from the Japan Society for the Promotion of Science (Grant nos. 17K06173, 18K03958, and 18H01135).

References

[1] R.P. Chhabra, Bubbles, Drops, and Particles in Non-Newtonian Fluids, 2 edition, CRC Press, Boca Raton, FL, 2006.
[2] R. Zenit, J.J. Feng, Hydrodynamic interactions among bubbles, drops, and particles in non-Newtonian liquids, Annu. Rev. Fluid Mech. 50 (2018) 505–534, doi:10.1146/annurev-fluid-122316-045114.
[3] R. Cressely, R. Hocquart, Biréfringence d'écoulement localisée induite á l'arriére d'obstacles, Opt. Acta 27 (1980) 699–711, doi:10.1080/713820288.
[4] G.H. McKinley, R.C. Armstrong, R.A. Brown, The wake instability in viscoelastic flow past confined circular cylinders, Philos. Trans. R. Soc. Lond. A 344 (1671) (1993) 265–304, doi:10.1098/rsta.1993.0091.
[5] A.H. Shiang, A. Öztekin, J.-C. Lin, D. Rockwell, Hydroelastic instabilities in viscoelastic flow past a cylinder confined in a channel, Exp. Fluids 28 (2) (2000) 128–142, doi:10.1007/s003480050017.
[6] J.M. Verhelst, F.T.M. Nieuwstadt, Visco-elastic flow past circular cylinders mounted in a channel: experimental measurements of velocity and drag, J. Non-Newton. Fluid Mech. 116 (2–3) (2004) 301–328, doi:10.1016/j.jnnfm.2003.08.006.
[7] C.J. Pipe, P.A. Monkewtiz, Vortex shedding in flows of dilute polymer solutions, J. Non-Newton. Fluid Mech. 139 (1–2) (2006) 54–67, doi:10.1016/j.jnnfm.2006.07.003.
[8] G.R. Moss, J.P. Rothstein, Flow of wormlike micelle solutions past a confined circular cylinder, J. Non-Newton. Fluid Mech 165 (21–22) (2010) 1505–1515, doi:10.1016/j.jnnfm.2010.07.014.

[9] V.M. Ribeiro, P.M. Coelho, F.T. Pinho, M.A. Alves, Viscoelastic fluid flow past a confined cylinder: three-dimensional effects and stability, Chem. Eng. Sci. 111 (2014) 364–380, doi:10.1016/j.ces.2014.02.033.
[10] D.F. James, T. Shiau, P.M. Aldridge, Flow of a Boger fluid around an isolated cylinder, J. Rheol. 60 (6) (2016) 1137–1149, doi:10.1122/1.4961482.
[11] M.D. Chilcott, J.M. Rallison, Creeping flow of dilute polymer solutions past cylinders and spheres, J. Non-Newton. Fluid Mech. 29 (1–3) (1988) 381–432, doi:10.1016/0377-0257(88)85062-6.
[12] M.A. Alves, F.T. Pinho, P.J. Oliveira, The flow of viscoelastic fluid past a cylinder: finite-volume high-resolution methods, J. Non-Newton. Fluid Mech. 97 (2–3) (2001) 207–232, doi:10.1016/S0377-0257(00)00198-1.
[13] P.J. Oliveira, A.I.P. Miranda, A numerical study of steady and unsteady viscoelastic flow past bounded cylinders, J. Non-Newton. Fluid Mech. 127 (1) (2005) 51–66, doi:10.1016/j.jnnfm.2005.02.003.
[14] T.M. Squires, S.R. Quake, Microfluidics: fluid physics at the nanoliter scale, Rev. Mod. Phys. 77 (2005) 977–1026.
[15] N. François, D. Lasne, Y. Amarouchene, B. Lounis, H. Kellay, Drag enhancement with polymers, Phys. Rev. Lett. 100 (1) (2008) 018302, doi:10.1103/PhysRevLett.100.018302.
[16] S. Kenney, K. Poper, G. Chapagain, G.F. Christopher, Large Deborah number flows around confined microfluidic cylinders, Rheol. Acta 52 (5) (2013) 485–497, doi:10.1007/s00397-013-0712-8.
[17] L. Pan, A. Morozov, C. Wagner, P.E. Arratia, Non-linear elastic instability in channel flows at low Reynolds number, Phys. Rev. Lett. 110 (17) (2013) 174502, doi:10.1103/PhysRevLett.110.174502.
[18] F.J. Galindo-Rosales, L. Campo-Deaño, P.C. Sousa, V.M. Ribeiro, M.S.N. Oliveira, M.A. Alves, F.T. Pinho, Viscoelastic instabilities in micro-scale flows, Exp. Them. Fluid Sci. 59 (2014) 128–139, doi:10.1016/j.expthermflusci.2014.03.004.
[19] X. Shi, S. Kenney, G. Chapagain, G.F. Christopher, Mechanisms of onset for moderate mach number instabilities of viscoelastic flows around confined cylinders, Rheol. Acta 54 (9–10) (2015) 805–815, doi:10.1007/s00397-015-0875-6.
[20] X. Shi, G.F. Christopher, Growth of viscoelastic instabilities around linear cylinder arrays, Phys. Fluids 28 (12) (2016) 124102, doi:10.1063/1.4968221.
[21] Y. Zhao, A.Q. Shen, S.J. Haward, Flow of wormlike micellar solutions around confined microfluidic cylinders, Soft Matter 12 (42) (2016) 8666–8681, doi:10.1039/c6sm01597b.
[22] C.-L. Sun, H.-Y. Huang, Measurements of flow-induced birefringence in microfluidics, Biomicrofluidics 10 (1) (2016) 011903, doi:10.1063/1.4939949.
[23] K.P. Nolan, A. Agarwal, S. Lei, R. Shields, Viscoelastic flow in an obstructed microchannel at high Weissenberg number, Microfluid. Nanofluid. 20 (7) (2016) 101, doi:10.1007/s10404-016-1765-7.
[24] A. Varshney, V. Steinberg, Elastic wake instabilities in a creeping flow between two obstacles, Phys. Rev. Fluids 2 (7) (2017) 05130, doi:10.1103/PhysRevFluids.2.051301.
[25] B. Qin, P.E. Arratia, Characterizing elastic turbulence in channel flows at low Reynolds number, Phys. Rev. Fluids 2 (8) (2017) 083302, doi:10.1103/PhysRevFluids.2.083302.
[26] C. Li, B. Qin, A. Gopinath, P.E. Arratia, B. Thomases, R.D. Guy, Flagellar swimming in viscoelastic fluids: role of fluid elastic stress revealed by simulations based on experimental data, J. R. Soc. Interface 14 (135) (2017) 20170289, doi:10.1098/rsif.2017.0289.
[27] N. Burshtein, S.T. Chan, K. Toda-Peters, A.Q. Shen, S.J. Haward, 3D-printed glass microfluidics for fluid dynamics and rheology, Curr. Opin. Coloid Int. 43 (2019) 1–14, doi:10.1016/j.cocis.2018.12.005.
[28] S.J. Haward, K. Toda-Peters, A.Q. Shen, Steady viscoelastic flow around high-aspect-ratio, low-blockage-ratio microfluidic cylinders, J. Non-Newton. Fluid Mech. 254 (2018) 23–35, doi:10.1016/j.jnnfm.2018.02.009.
[29] S.J. Haward, N. Kitajima, K. Toda-Peters, T. Takahashi, A.Q. Shen, Flow of wormlike micellar solutions around microfluidic cylinders with high aspect ratio and low blockage ratio, Soft Matter 15 (2019) 1927–1941, doi:10.1039/c8sm02099j.
[30] R.W. Mair, P.T. Callaghan, Observation of shear banding in worm-like micelles by NMR velocity imaging, Europhys. Lett. 36 (1996) 719–724, doi:10.1209/epl/i1996-00293-9.
[31] S.M. Fielding, Triggers and signatures of shear banding in steady and time-dependent flows, J. Rheol. 60 (2016) 821–834, doi:10.1122/1.4961480.
[32] A.A. Dey, Y. Modarres-Sadeghi, J.P. Rothstein, Viscoelastic fluid-structure interactions between a flexible cylinder and wormlike micelle solution, Phys. Rev. Fluids 3 (2018) 063301, doi:10.1103/PhysRevFluids.3.063301.
[33] A.A. Dey, Y. Modarres-Sadeghi, J.P. Rothstein, Experimental observation of viscoelastic fluid-structure interactions, J. Fluid Mech. 813 (2017) R5, doi:10.1017/jfm.2017.15.
[34] C.C. Hopkins, S.J. Haward, A.Q. Shen, Purely elastic fluidstructure interactions in microfluidics: implications for mucociliary flows, Small (2019) 1903872, doi:10.1002/smll.201903872.
[35] M. Müller, J. Vorwerk, P.O. Brunn, Optical studies of local flow behaviour of a non-Newtonian fluid inside a porous medium, Rheol. Acta 37 (1998) 189–194, doi:10.1007/s003970050105.
[36] S. De, J. van der Schaaf, N.G. Deen, J.A.M. Kuipers, E.A.J.F. Peters, J.T. Padding, Lane change in flows through pillared microchannels, Phys. Fluids 29 (11) (2017) 113102, doi:10.1063/1,4995371.
[37] J. Gottmann, M. Hermans, J. Ortmann, Digital photonic production of micro structures in glass by in-volume selective laser-induced etching using a high speed micro scanner, Phys. Proc. 39 (2012) 534–541, doi:10.1016/j.phpro.2012.10.070.
[38] G. Meineke, M. Hermans, J. Klos, A. Lenenbach, R. Noll, A microfluidic opto-caloric switch for sorting of particles by using 3D-hydrodynamic focusing based on SLE fabrication capabilities, Lab Chip 16 (5) (2016) 820–828, doi:10.1039/C5LC01478F.
[39] A.V. Dobrynin, R.H. Colby, M. Rubinstein, Scaling theory of polyelectrolyte solutions, Macromolecules 28 (6) (1995) 1859–1871, doi:10.1021/ma00110a021.
[40] V. Sharma, G.H. McKinley, An intriguing empirical rule for computing the first normal stress difference from steady shear viscosity data for concentrated polymer solutions and melts, Rheol. Acta 51 (6) (2012) 487–495, doi:10.1007/s00397-011-0612-8.
[41] S.J. Haward, G.H. McKinley, Stagnation point flow of wormlike micellar solutions in a microfluidic cross-slot device: effects of surfactant concentration and ionic environment, Phys. Rev. E 85 (2012) 031502, doi:10.1103/PhysRevE.85.031502.
[42] W.P. Cox, E.H. Merz, Correlation of dynamic and steady flow viscosities, J. Polym. Sci. 28 (1958) 619–622, doi:10.1002/pol.1958.1202811812.
[43] V.M. Entov, E.J. Hinch, Effect of a spectrum of relaxation times on the capillary thinning of a filament of elastic liquid, J. Non-Newton. Fluid Mech. 72 (1997) 31–54, doi:10.1016/S0377-0257(97)00022-0.
[44] S.L. Anna, G.H. McKinley, Elasto-capillary thinning and breakup of model elastic liquids, J. Rheol. 45 (1) (2001) 115–138, doi:10.1122/1.1332389.
[45] C.D. Meinhart, S.T. Wereley, M.H.B. Gray, Volume illumination for two-dimensional particle image velocimetry, Meas. Sci. Technol. 11 (6) (2000) 809–814, doi:10.1088/0957-0233/11/6/326.
[46] A. Groisman, V. Steinberg, Efficient mixing at low reynolds number using polymer additives, Nature 410 (2001) 905–908, doi:10.1038/35073524.
[47] P.C. Sousa, F.T. Pinho, M.A. Alves, Purely-elastic flow instabilities and elastic turbulence in microfluidic cross-slot devices, Soft Matter 14 (2018) 1344–1354, doi:10.1039/c7sm01106g.
[48] L. Casanellas, M.A. Alves, R.J. Poole, S. Lerouge, A. Lindner, The stabilizing effect of shear thinning on the onset of purely elastic instabilities in serpentine microflows, Soft Matter 12 (2016) 6167–6175, doi:10.1039/c6sm00326e.